European Journal of Mechanics / A Solids 101 (2023) 105057

Contents lists available at ScienceDirect

European Journal of Mechanics / A Solids

journal homepage: www.elsevier.com/locate/ejmsol

On the use of *in situ* X-ray computed tomography for soft contact mechanics

Vito Acito [a,b,*], Sylvain Dancette [b,c], Julien Scheibert [a], Cristobal Oliver [a], Jérome Adrien [b], Eric Maire [b], Davy Dalmas [a,**]

[a] Univ Lyon, CNRS, Ecole Centrale de Lyon, ENTPE, LTDS, UMR5513, Ecully, 69130, France
[b] Laboratoire MATEIS UMR CNRS 5510, Univ Lyon, INSA Lyon, Villeurbanne, F-69621, France
[c] ELyTMaX IRL3757, CNRS, Univ Lyon, INSA Lyon, Centrale Lyon, Université Claude Bernard Lyon 1, Tohoku University, Sendai, 980-8577, Japan

ARTICLE INFO

Keywords:
Tribology
Contact area
Surface deformation
Elastomer
Image segmentation
Adhesion

ABSTRACT

The real contact area A_R between two solids in contact is an outstanding quantity that controls the frictional and adhesive behavior of a contact interface. Most of the experimental methods to measure A_R are based on the contrast in local optical properties of the interface, between in- and out-of-contact regions. Although those methods recently enabled various new insights into contact mechanics and tribology, they suffer from important limitations: they require that at least one of the two solids is optically transparent; they only provide information about the real interface, including A_R, but not to the bulk deformation that is at the origin of A_R. Here, we propose *in situ* X-ray Computed Tomography (XRCT) as an appealing alternative method to overcome those limitations. Indeed, it enables three-dimensional access to interfaces within potentially non-transparent contact pairs. We test the advantages and disadvantages of the method on the smooth contact between a smooth elastomer sphere in contact against a smooth rigid plate. Such a tribological system is chosen because the real contact area measurement can be benchmarked against standard optical results. We show that XRCT can, in addition, give unique access to the full surface deformation of the solids in contact, opening the way to deeper comparisons with existing models of adhesive spherical contacts.

1. Introduction

A good understanding of the tribological behavior (e.g. friction and adhesion) of contact interfaces involving soft materials (e.g. gels, elastomers and human skin) is required in a variety of systems, either natural (e.g. fingertip/textured surface Scheibert et al., 2009) or engineered (e.g. tire/road Persson et al., 2004 and soft robotics Mengaldo et al., 2022). A critical quantity that controls the mechanical response of a contact interface is the so-called real contact, *i.e.* where the two solids are in intimate contact. For instance, the friction force is often proportional to the total area of real contact A_R (Bowden and Tabor, 1942; Sahli et al., 2018). Other morphological features of the real contact, e.g. its potential anisotropy (Sahli et al., 2019; Putignano et al., 2019), affect most of the macroscopic responses of the interface, including thermal or electrical conductivities (Popov, 2017), contact stiffnesses (Medina et al., 2013) or wear (Aghababaei et al., 2017). The real contact morphology depends on (i) the intrinsic features of the individual solids, including their elastic moduli, macroscopic shape and surface roughness (see Vakis et al. (2018) for a review), (ii) the interactions between their surfaces, adhesion in particular (Maugis, 1992), and (iii) the loading conditions, including the normal (Dieterich and Kilgore, 1994) and shear forces (Sahli et al., 2018) and the time elapsed since contact creation (Dieterich and Kilgore, 1994). All those dependencies and their potential interplay make it difficult to predict the real contact of a given system, so that experimental measurements remain necessary.

The measurement of the real contact area, A_R, is then of strong importance in understanding the adhesive and shear-resistance properties of a contact interface. However, despite a significant number of numerical or analytical contact models available in the literature (Müser et al., 2017; Vakis et al., 2018), experimental measurements of A_R are still challenging. Up to now, the vast majority of A_R measurements have been made using optics-based setups offering a contrast between the real contact area and the rest of the interface (out-of-contact regions) (Dieterich and Kilgore, 1994; Rubinstein et al., 2006; Chateauminois et al., 2010; Krick et al., 2012; Prevost et al., 2013; Dalzin et al., 2016; Sahli et al., 2019; Acito et al., 2019; Lengiewicz et al., 2020). In such experimental studies, the use of at least one optically transparent material is required and strongly limits the number of systems that can be analyzed, by excluding opaque materials. Another limitation is that, in most cases, only the 2D projected area of contact

* Corresponding author at: Univ Lyon, CNRS, Ecole Centrale de Lyon, ENTPE, LTDS, UMR5513, Ecully, 69130, France.
** Corresponding author.
E-mail addresses: vito.acito@ec-lyon.fr (V. Acito), davy.dalmas@ec-lyon.fr (D. Dalmas).

https://doi.org/10.1016/j.euromechsol.2023.105057
Received 17 January 2023; Received in revised form 10 May 2023; Accepted 9 June 2023
Available online 12 June 2023

is available. In practice, it is usually unsuitable for non-planar contact interfaces having an out-of-plane extension larger than the depth of field of the optical setup (for instance contacts between a rigid sphere and a compliant plane, under a large normal load). Even for planar contacts, the out-of-contact surfaces around the real contact are often, depending on the optical method used, either non-detected (e.g. when real contact is imaged by total internal reflection Rubinstein et al., 2006) or out-of-focus (Lengiewicz et al., 2020). Thus, optical methods generally limit the analysis of the contact state to the evolution of A_R, hindering any access to the full surface displacement field that accompanies the creation of the real contact.

In this study, we aim at overcoming the above-mentioned limitations by using an X-ray Computed Tomography (XRCT) method to investigate the contact between two solids in 3D. Indeed, XRCT constitutes a promising characterization method when it comes to non-destructive, *in situ* or *in operando* three-dimensional observation of a contact interface. We expect it to overcome the limits of optical transparency, with the additional benefit of giving access to a full 3D observation of the vicinity of the contact zone (out-of-contact regions). XRCT is classically used to characterize the 3D *volume* of a specimen in a non-destructive way: the specimen is placed between an X-ray source and a detector and a series of radiographs are taken during its step-by-step rotation; then, well-established algorithms enable reconstruction of the 3D volume from the numerous 2D projections of the specimen (Withers et al., 2021). 3D rendering of the solids' surfaces or internal interfaces in multiphase materials can be obtained by surface extraction techniques, based for example on the Marching Cube algorithm (Lorensen and Cline, 1987). Only a few studies in the literature attempted to use XRCT to image the morphology of two non-optically transparent surfaces in contact. Zhang et al. (2019) and Zhang et al. (2020) (for rough metallic contact) and Kriston et al. (2016) (for rough rubber contact) mainly focused on the evaluation of A_R and surface separation. Aleksejev et al. (2020) used XRCT instead of *post-mortem* measurements to evaluate the wear state of two contacting bodies. In all these studies, the analyses were carried out on complex surfaces without carrying out a preliminary and necessary examination of the limits of XRCT; such as estimating the errors in the measurement of the contact area.

Thus, the question addressed in this work is whether or not the XRCT technique, developed for 3D observation of *volumes*, can be reliably used for 3D observation of *interfaces* and *quantitative* measurement of the real contact area A_R in tribological systems. We focus here on the *in situ* measurement of the evolution of A_R during a compression test (normal loading) performed on a model system consisting of a soft smooth sphere in contact with a rigid smooth plane. Such a system has been chosen because it is adapted to the constraints of X-ray tomography but can also be investigated using more classical optical devices. This allows us to benchmark our XRCT A_R measurements against an already mastered 2D optomechanical device (Guibert et al., 2021). In the framework of this type of contact, the apparent contact area is coincident to the real contact area but the same considerations may be applied to more realistic rough contacts (where A_R is much smaller than A_A). Finally, based on such 3D images of our model contact system, we will show that we can extract the 3D surface displacement field and compare it to the predictions of the most used theoretical models of adhesive contact mechanics (Barthel, 2008; Maugis, 1992).

2. Materials and methods

2.1. Sphere-on-plane contact specimens

The investigated tribological system consists of a soft hemisphere in contact with a stiff plate. While little preparation was needed for the stiff body, made of 5 mm-thick PMMA (Polymethyl methacrylate) plate cut to a diameter of 20 mm, the soft hemisphere was made of a PDMS (Polydimethylsiloxane) specimen specially designed for the experiment.

The PDMS material is a Sylgard 184 silicone (®™Dow Corning) known for its low Young's modulus, large toughness, good chemical resistance and optical transparency (Delplanque et al., 2022). In terms of tribological interests, PDMS was chosen for its transparency and low modulus. The first property allowed us to compare the XRCT results with already mastered optical measurements of the contact area, while the second one permitted us to get a large and observable contact area compatible with the resolution of our tomograph. Sylgard 184 was supplied as a two-part liquid component kit: a pre-polymer base and a curing agent that were mixed with a mass ratio of 20:1. The liquid mixture was also charged with hollow micrometric glass beads (K15, 3M™), filtered to an external diameter between 80 μm and 100 μm and mixed with a volume fraction of 7.17% inside the PDMS matrix. Such beads are intended to be used as markers for Digital Volume Correlation in an upcoming study. Nevertheless, an external superficial thin film of pure PDMS was added on the exterior surface of the hemisphere to promote smooth contact with the PMMA plate and to prevent the presence of beads at the extreme surface, which would have an influence on the contact behavior.

Fig. 1 depicts the sample preparation procedure. First, a small drop of pure PDMS is deposited in a smooth concave glass lens (9.42 mm radius of curvature, model 45-014, Edmund Optics®) inserted in a 12 mm-diameter cylindrical mould. Then, a spin coater (model SPIN 150, APT GmbH) is used to spread the drop and produce a 30 μm thick film of pure PDMS, reticulated for 10 min at 80 °C. The remaining volume of the cylinder is then filled with the PDMS mixture with glass beads and is subsequently reticulated for 1.5 h at 80 °C to reach a complete cross-linking. Note that the mould, covered by a glass plate, is rotated every 10 min during reticulation (see blue arrow in Fig. 1(b)) in order to obtain a homogeneous dispersion of glass beads in the bulk. The resulting PDMS sample shows an apparent Young's modulus $E \simeq 0.7$ MPa and a work of adhesion $w \simeq 0.06$ J/m^2. The method to extract the Young's modulus and the work of adhesion from compression tests is provided in Section 2.3.2.

The specimens elaborated in the present work were designed for the *in situ* tomography procedure presented in the next section, but they also comply with the experimental set-up used for the optical measurement of A_R and detailed in Section 2.3.2.

2.2. In situ compression test under X-ray tomography

The tomograph used in this work was a V-TomeX device (GE Phoenix X-ray GmbH) with a 2520 V detector from Varian (Pixel matrix 1920 × 1536, pixel pitch 127 μm^2). 900 radiographs with an exposure time of 999 ms (averaging 3 images with an exposure of 333 ms for each image) were taken during the 360° rotation of the specimen. This dwell time was chosen as an optimization of two effects. If the time is too short, the signal on the detector would be insufficient with a low value of the signal to noise ratio and a low-quality reconstructed volume. Conversely, an high exposure time would extend too much the time required to complete a scan with a possible important relaxation of the body and the presence of blurring in the image. The polychromatic conical X-ray beam was produced at 80 kV and 280 mA. The 3 radiographs averaged at each angular step reduced the noise and lead to a total acquisition time of 20 min for each volume. Reconstruction of the 3D volumes was obtained with the filtered back-projection algorithm (Feldkamp et al., 1984) available with the tomograph. The 16-bit gray level volumes provided by the reconstruction algorithm were subsequently converted to 8-bit for further image visualization and processing.

The experimental setup is shown in Fig. 2. An *in situ* compression device was used to carry out normal loading experiments (Buffiere et al., 2010), installed on a 4-axes moving stage between the X-ray tube and the detector. The PDMS sample of Fig. 1(c) was screwed on the lower moving rod of the compression device. On the other side of the rod, a motorized vertical translating stage imposed the z-displacement

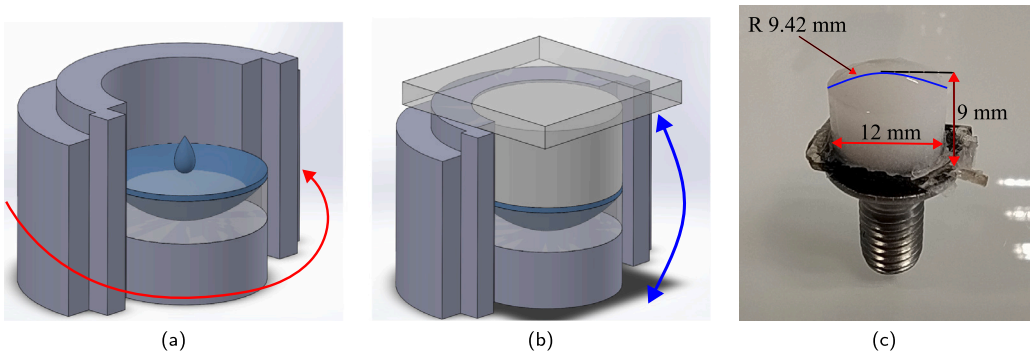

Fig. 1. Sample preparation in a cylindrical mould equipped with a concave lens. (a) A drop of pure PDMS is deposited in the lens, spin-coated and reticulated at 80 °C for 10 min to produce a thin superficial film. (b) The liquid PDMS mixture containing hollow glass particles is poured into the mould, which is then covered with a glass plate and reticulated at 80 °C for 90 min to form the bulk. Alternative rotations (see blue arrow) allowed a homogeneous dispersion of the glass beads. (c) Final sample with the relevant dimensions. The whitish color is due to the presence of glass beads in the bulk. After reticulation, the sample is glued on an M8 countersunk screw for easy installation in the compression device. (For interpretation of the references to color in this figure legend, the reader is referred to the web version of this article.)

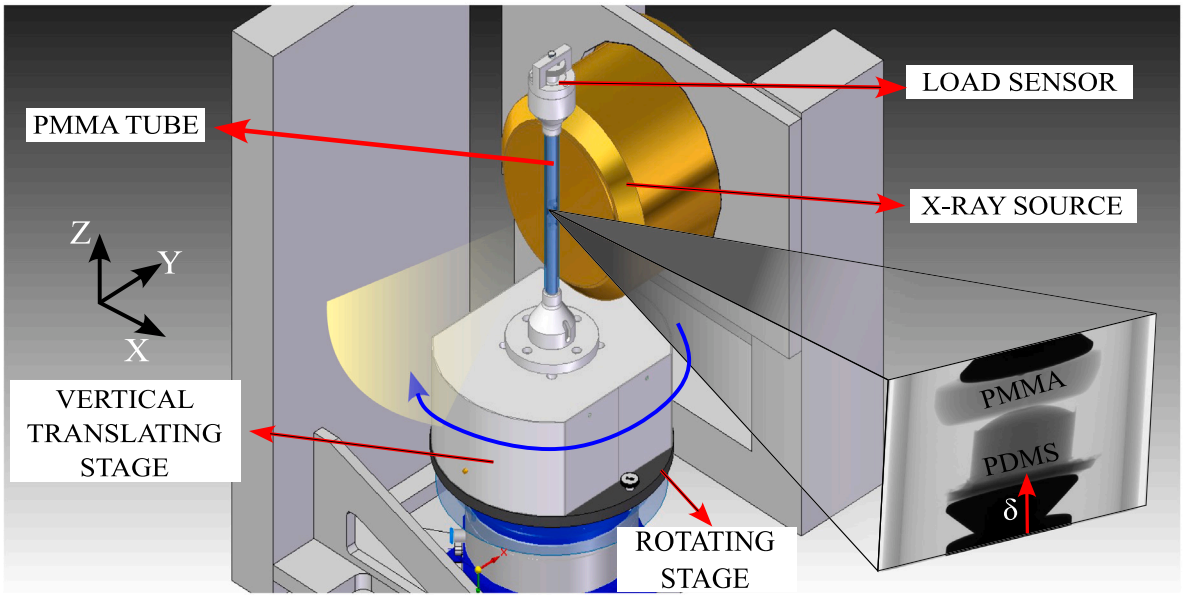

Fig. 2. Schematic view of the compression device installed in the tomograph. The two bodies in contact are installed inside the compression device where a displacement can be imposed through a motorized vertical translating stage (not visible in the current image). While the materials are exposed to X-rays, the entire device rotates 360° to acquire projections (called radiographs) of the specimens at different angles. The inset on the right shows one of the radiographs collected during a scan at low resolution to visualize the two materials in contact with the upper and lower rods of the compression device. In the present configuration, the PMMA disk is fixed while the displacement is imposed on the PDMS specimen.

during the experiments. The PMMA plate was glued to the fixed upper rod, which was connected to a 200 N load sensor with a sensitivity of 0.008 N. A PMMA tube (external diameter 30 mm, internal diameter 26 mm) connected the upper and lower parts of the compression device to allow the transmission of forces to the interface. Note that the outer diameter of the tube constrained the minimum distance between the specimen and the X-ray source. In the optimal configuration, *i.e* with the sample as close as possible to the X-ray source, the voxel size was 4 μm. The resulting field of view close to the contact zone was $6.8 \times 6.8 \times 2.8$ mm^3. In this *local tomography* configuration, the object is larger than the field of view of the detector.

The compression tests were carried out step by step under controlled displacement with 20 μm steps from 0 up to 160 μm (loading) and back to −10 μm (unloading). Due to the quasi-static conditions required by the XRCT technique (20 min scans at each loading step), a dwell time was required to prevent any significant visco-elastic relaxation of the PDMS during the scans, avoiding therefore potential image blurring and variation of A_R during the acquisition of images. An optimum waiting time of 5 min was applied before scanning at each load step. This optimal time was found thanks to an additional optical experiment at imposed load during which we followed the evolution of A_R. It showed that the variation of A_R was negligible after 5 min compared to the resolution of the tomography measurement. The temperature inside the tomograph was controlled through a cooling system regulating the X-ray tube so that temperature elevation of the ambient air in the lead cabin should be less than one degree. In the present case, our experiments were carried out at 25 °C.

2.3. Contact area measurements

2.3.1. 3D surface extraction from X-ray computed tomography

The goal of the procedure developed here is to compute the real contact area A_R for each volume acquired during the *in situ* compression test. This is carried out by image analysis performed on the gray-level volumes resulting from the tomography reconstruction process.

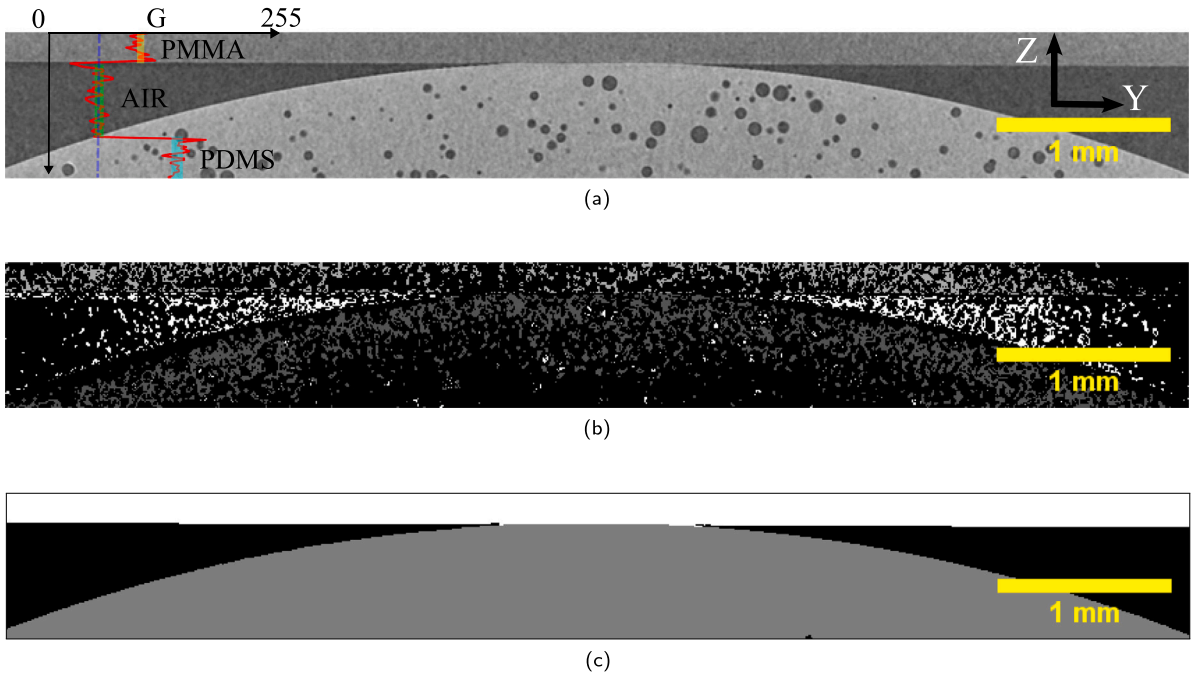

Fig. 3. Illustration of the segmentation process. (a) Original volume together with a representation of the gray-level G in red taken along the dashed blue line crossing all three phases (PMMA in gray, air in dark gray and PDMS in light gray). (b) Positioning of markers for the different materials, corresponding to voxels with a gray level equal to the average value in each phase - extracted from the red profile in the image (a) - plus or minus a tolerance of 10% (colored bands: yellow for PMMA, Green for air and blue for PDMS). (c) Labeled volume obtained with the Random Walker Segmentation algorithm with air in black, PMMA in white and PDMS in gray. (For interpretation of the references to color in this figure legend, the reader is referred to the web version of this article.)

The first step consists of a segmentation task to label each voxel of the volumes. We have adopted the Random Walker Segmentation (Grady, 2006) method, as implemented in the python `scikit-image` package (Walt et al., 2014), to separate the different phases in the volumes, namely air, PMMA and PDMS materials. Starting from a set of labeled markers for each phase, an anisotropic diffusion equation is solved where the diffusion coefficient depends on the gradients in the gray level. Diffusion is facilitated if neighboring voxels present similar gray values and it is penalized by the presence of high gradients. In the end, the label of each voxel corresponds to the one of the known marker that has the highest probability to reach it during the diffusion process. The algorithm was run with a penalty coefficient $\beta = 10^4$ for the diffusion.

Fig. 3 shows how the algorithm performed the segmentation task. The first step consisted in assigning a label to the markers, defined as a limited set of voxels belonging to one of the three phases without ambiguity. To do so, we started by extracting the gray-level G from a vertical profile in the 3D volume, judiciously chosen to cross the three phases (see the blue superimposed dashed line in Fig. 3(a)). In this way, an average gray value could be calculated for each phase. The markers of a given phase thus corresponded to all voxels of the volume with a gray level equal to the average value plus or minus a tolerance of 10% (see the narrow colored bands superimposed on the gray-level profile). The markers obtained from this step are illustrated in Fig. 3(b). Finally, the diffusion process with the Random Walker algorithm produces the segmented volume of Fig. 3(c), where each voxel shows a unique label corresponding here to either air (in black), PMMA (in white) or PDMS (in gray).

Starting from the labeled volume of the contact specimen at a given load, 3D surface reconstruction was used to extract the contact area. The procedure is based on a multi-material extension of the marching cubes algorithm (Lorensen and Cline, 1987; Wu and Sullivan, 2003). The latter is available for example in the commercial Avizo software (ThermoFisher Scientific) and is valid for any complexity of the contact surface. The algorithm creates a surface mesh of the boundaries of the materials with triangular elements, where the characteristic length of the triangles is the voxel edge. The global surface mesh is partitioned into several surface patches depending on the materials on both sides of the boundary. In the present case, the contact area corresponds to the surface patch at the boundary between PMMA and PDMS, from which the real contact area A_R can be computed by summing the area of those triangles. Note that surface simplification or remesh (e.g. with a characteristic length of the triangles set to 4-times the voxel size) does not affect the computed contact area, as long as the chosen element size remains sufficiently fine to preserve the morphology of the surface.

Fig. 4 shows an example of surface extraction at a 152 μm contact displacement. Fig. 4(a) shows a 3D rendering of the boundary surfaces. Beyond the outer surfaces of the specimen (interfaces of the materials with the exterior), semi-transparency allows for the distinction of the boundary surface between PDMS and PMMA. Isolating the surface patch corresponding to the PDMS/PMMA interface, as in Fig. 4(b), allows the computation of the real contact area A_R. Even if it reduces to a planar contact surface in the present case, the procedure would allow us to compute it based on the real 3D topology of the interface in arbitrary complex tribological systems.

The two red circles superimposed in Fig. 4(b) highlight the limits of the presented procedure based on 3D image segmentation and surface extraction. Indeed, contrary to the prediction of contact mechanics equations (Johnson, 1987) in the case of a smooth isotropic soft sphere in contact with a smooth rigid plane, the contact area of Fig. 4(b) is not perfectly circular: the global shape is isotropic but the contour is not perfectly smooth and exhibits an irregular border with an apparent roughness. The two red circles connect respectively the peaks and the valleys of the irregular contact border. They are used in the following to define an upper and a lower bound of the 3D measurement of A_R.

The origin of the irregular border of the contact zone in Fig. 4(b) is mainly related to the presence of image artifacts in our tomography volumes (Barrett and Keat, 2004). These are illustrated in Fig. 5 where some streaks, starting from the boundary of the PDMS sphere, become more and more visible when approaching the contact plane. There are several possible reasons for the presence of such streaks. All of them

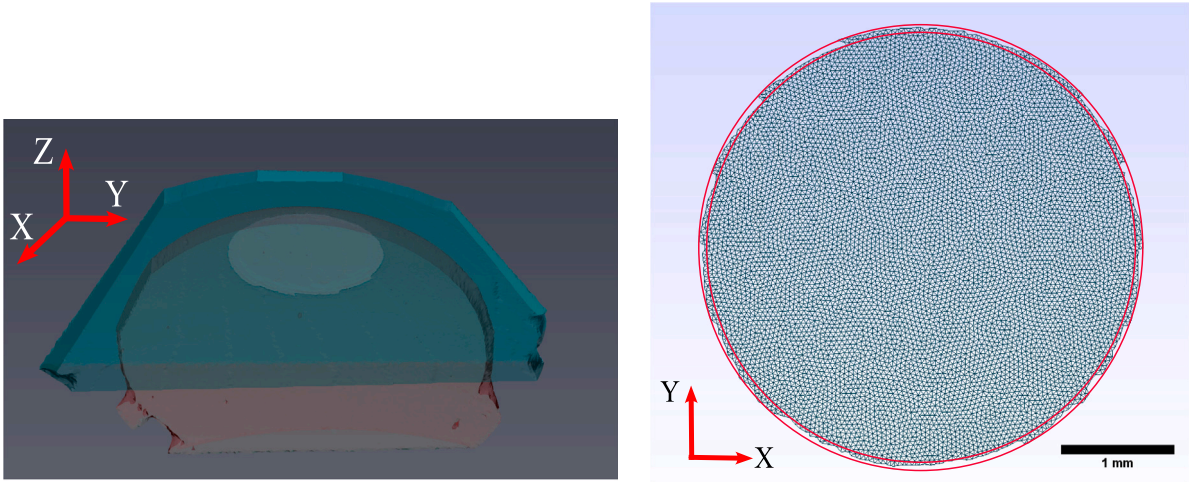

Fig. 4. Extraction of the contact area. (a) 3D rendering of the specimen surfaces at 152 μm contact displacement. Semi-transparency allows the identification of the contact surface at the PDMS/PMMA boundary. (b) Contact surface mesh extracted from the specimen surfaces. The external and internal red circles (connecting peaks and valleys on the contact border) are used to define an upper bound and a lower bound of the 3D contact area measurement. (For interpretation of the references to color in this figure legend, the reader is referred to the web version of this article.)

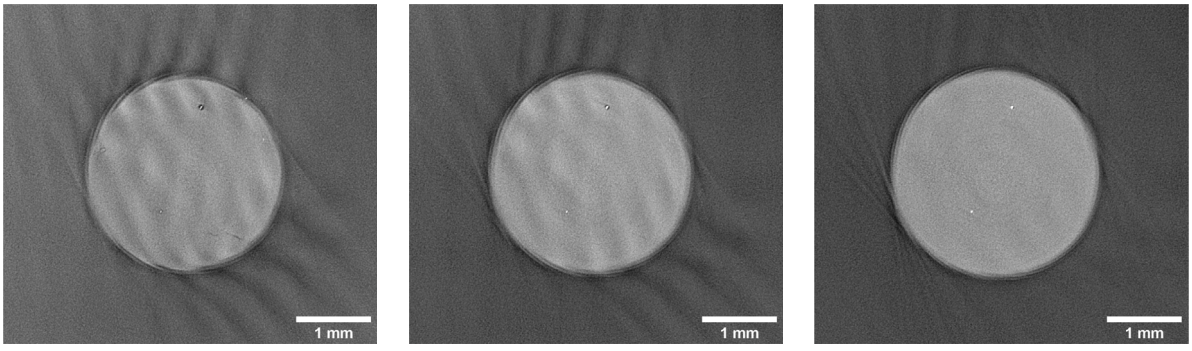

Fig. 5. Artifacts near the contact zone in horizontal slices extracted from the 3D volume at increasing distance from the PMMA surface (4 μm, 8 μm and 12 μm), i.e. moving downwards from the contact plane into PDMS. The images correspond to a volume taken at an indentation of 152 μm.

essentially arise from the fact that the contact surface was contained in a plane roughly parallel to the propagation direction of the X-rays.

- First, this geometrical configuration promoted the building of the so-called "phase contrast" (see Cloetens et al. (1997)). Although less problematic on laboratory tomographs than on synchrotron beamline, phase contrast was likely to be more important in the present case because of the long propagation distance of the X-rays on each side of a dissimilar interface. The intensity of phase contrast might even lead to saturation of our detector in some particular angles and this could have caused a well-known "streak artifact" (see Barrett and Keat (2004)). Because the tomograph's reconstruction algorithm only accounts for the attenuation of the X-rays (and not phase shift), this extra phase contrast likely perturbed our segmentation.
- Second, a planar surface is always difficult to capture using a discrete referential, such as a grid of voxels. For instance, in the situation where the surface is only slightly misaligned with the reference plane defined by the voxels grid, the segmented surface will present regular steps, of 1 voxel of height, following the tilting of the plane. These steps were particularly visible at the periphery of the surface that we wanted to capture (see for example the steps leading to the perturbation of the outer circle clearly visible in Fig. 4(b)).

We have attempted different experimental adjustments and trials to mitigate and reduce these irregularities. Firstly we increased the number of projections (1500 instead of 900). We also attempted to shift the rotation axis away from the middle of the detector or to increase the voltage on the X-ray source (in order to reduce phase contrast). We imposed an angle to the compressing machine (to reduce the parallelism of the interface with the beam propagation), and we also machined the edges of the PMMA disk (to reduce the propagation distance by reducing the dimension of the PMMA/air plane). Even if the effects were not remarkable, in the sense that they only slightly reduced the imperfections, we present in this paper the volume obtained with the optimal configuration we found.

2.3.2. 2D optical reference measurement

In order to compare the 3D XRCT measurements of A_R with measurements resulting from an optical method, similar compression tests were performed using an optomechanical device, described in section III.B of Guibert et al. (2021). We carried out compression tests using the same PDMS sphere and PMMA plane using the same kinematics as for XRCT compression tests (see Section 2.2). In particular, we used the same dwell time of 5 min between successive indentation steps of 2 μm (this small indentations allow to increase the number of measurement and thus the resolution in the evaluation of the mechanical properties of the PDMS). The measurement of the normal force was obtained

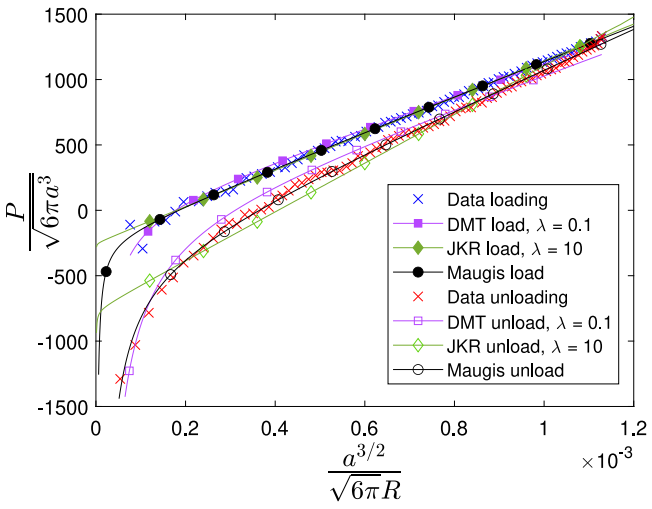

Fig. 6. Benchmark optical measurements of the PDMS sphere/PMMA plane contact under normal loading, using the same samples as in the tomography setup. Evolution of the normalized normal load versus the normalized contact radius during loading (blue crosses) and unloading (red crosses). The lines present the fits with 3 adhesive contact models during loading (solid markers) and unloading (open markers): JKR (Johnson et al., 1971) in green, DMT (Derjaguin et al., 1975) in purple and Maugis–Dugdale Maugis (1992) in black. (For interpretation of the references to color in this figure legend, the reader is referred to the web version of this article.)

using a 6-axes load cell, described in detail in Guibert et al. (2021). Those mechanical measurements were combined with *in-operando* visualization of the contact area. Using a high-resolution camera (Teledyne DALSA Genie Nano-GigE, 3008 × 4112 pixels) we acquired images of the contact interface with a spatial resolution of 3.3 μm/pixel. The contact area is measured with an image analysis method based on a fixed threshold to binarize the image (separate pixel in- from out-of-contact pixels), as already used in Sahli et al. (2018, 2019), Mergel et al. (2019) and Lengiewicz et al. (2020).

The error in the area measurements was estimated to be about 0.006 mm^2. This relatively small error comes from light intensity fluctuations on the periphery of the contact zone and it was estimated as the standard deviation of de-trended evolution (moving average over 5 five consecutive images) of the contact area values along the experiment.

Fig. 6 shows the evolution of the normalized normal force $P/\sqrt{6\pi a^3}$ as a function of the normalized contact radius $a^{3/2}/\sqrt{6\pi R}$ for the optical experiments during loading (blue crosses) and unloading (red crosses), with a the radius of the circular contact, P the contact's normal force and R the radius of curvature of the PDMS hemisphere. This normalization, proposed by Chaudhury et al. (1996), enables a simplified extraction of the contact parameters. Indeed, for a contact describable by the JKR theory (Johnson et al., 1971), the relationship between the normalized normal force and contact radius is affine. Its slope is directly related to Young's modulus, E, while the y-intercept is further related to the work of adhesion, w. The experimental data were fitted using three of the most used models of linearly elastic adhesive spherical contacts: (i) the JKR model (Johnson et al., 1971) which considers that adhesion acts only inside the area of contact, (ii) the DMT model (Derjaguin et al., 1975) which considers a displacement field identical to the non-adhesive case (Hertz model Johnson, 1987; Popov, 2017) but attractive interactions outside the area of contact and (iii) the Maugis–Dugdale model (Maugis, 1992) which unifies the two previous seemingly contradictory theories by taking into account the Tabor parameter λ (Tabor, 1977). This parameter allows a continuous transition between DMT regime for small λ (typically $\lambda < 0.1$) and JKR regime for large λ (typically $\lambda > 5$) (Barthel, 2008).

From a practical point of view, we use the equation proposed in the Maugis–Dugdale model (Maugis, 1992), with E and w as fitting parameters, to describe the normalized experimental values of Fig. 6 with either (i) $\lambda = 10$ for the JKR limit, (ii) $\lambda = 0.1$ for the DMT limit and (iii) λ as an additional fitting parameter for the Maugis–Dugdale model. The results are shown in Fig. 6 and the values of the fitting parameters are presented in Table 1 with the error bars being the 95% confidence interval. All three models seem to capture both the affine evolution at large contact load and the adhesion hysteresis (*i.e.* the different behavior during loading and unloading) that is attributed in the literature either to the presence of chemical heterogeneities (Sanner and Pastewka, 2022), to viscoelasticity (Violano et al., 2021) or to roughness (Pérez-Ràfols and Nicola, 2022). In contrast, only the DMT and the Maugis–Dugdale models seem to capture the lower cut-off (deviation from the line in Fig. 6, especially visible during unloading). As discussing in detail those results is not the objective of the present paper, in the following, we accounted for the difference during loading and unloading by directly using the values of Table 1 in our analysis and only focusing on the consequences on the contact area and surface deformation.

Table 1
Values and 95% confidence intervals of Young's modulus E, work of adhesion w and Tabor parameter λ (Tabor, 1977) resulting from fits based on Maugis' contact model (Maugis, 1992) of the evolution of the normalized contact load versus the normalized contact area during the compression of a PDMS sphere by a rigid plane. DMT and JKR limit regimes are obtained by imposing, respectively, a value of 0.1 and 10 for λ in the Maugis model. The fitted values are used to produce the theoretical deformation profiles in Fig. 12.

	E (10^5 Pa)	w (J/m^2)	λ
Maugis load	7.50 ± 0.16	0.059 ± 0.008	1.22 ± 0.51
Maugis unload	8.40 ± 0.14	0.305 ± 0.007	0.71 ± 0.06
DMT load	6.71 ± 0.09	0.095 ± 0.010	0.1
DMT unload	6.75 ± 0.16	0.292 ± 0.018	0.1
JKR load	7.79 ± 0.10	0.045 ± 0.004	10
JKR unload	10.43 ± 0.46	0.309 ± 0.038	10

3. Results and discussion

The tomography and surface reconstruction procedure introduced above gives access to several important quantities in the context of *in situ* contact mechanics. We focus in the following on two of these: (i) the evolution of the contact area and its accuracy (Section 3.1) and (ii) the surface displacement field and how it compares with theoretical predictions by classical linearly elastic adhesive contact models (Section 3.2). The latter, obtained from the deformed 3D surface of the PDMS hemisphere, constitutes a particularly innovative outcome of the present study, since it is not reachable with the reference optical *in situ* measurement.

3.1. Contact area

According to the XRCT method introduced before (Section 2.2), the evolution of contact area is plotted during loading (blue curve) and unloading (red curve) as a function of the normal indentation δ in Fig. 7(a) and of the normal load P in Fig. 7(b). This evolution of A_R exhibits a hysteresis between loading and unloading similar to that observed for optical measurement (see Fig. 6) (Sanner and Pastewka, 2022; Violano et al., 2021; Pérez-Ràfols and Nicola, 2022). However, contrary to the prediction from Hertz contact theory (Hertz, 1881), the relation between A_R and δ is not linear but affine (the intercept is not equal to 0) (Fig. 7(a)). The value of this intercept, which may be related to the effect of adhesion, is unexpectedly high. Indeed, in Fig. 8, the values of A_R from XRCT (middle blue curve with triangular markers) seem to be shifted upwards compared to optical measurement (purple curve). The origin of this discrepancy, both with the theoretical expectation and with the optical measurement is, in our opinion, mainly linked to a bias in the analysis of our XRCT experiments, as discussed in the following.

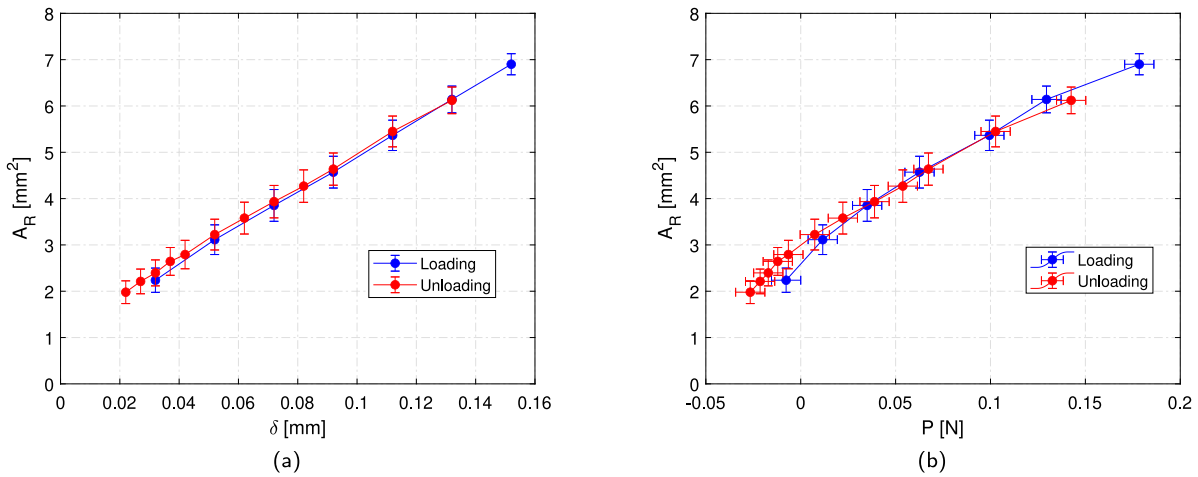

Fig. 7. Measured contact area from XRCT. (a) Measured contact area as a function of the normal indentation and (b) of the normal force. The contact area error bars are computed from the areas of the two circles fitting the peaks and valleys of the obtained contact contours (see Fig. 4). The force error bars correspond to the resolution of the normal force sensor. (For interpretation of the references to color in this figure legend, the reader is referred to the web version of this article.)

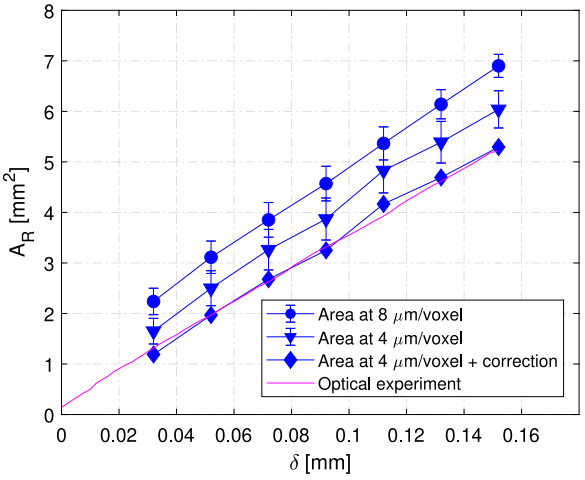

Fig. 8. Contact area as a function of the normal indentation for different resolutions of the tomography volumes (4 μm and 8 μm voxel size), compared with the optical measurement. The corrected 4 μm curve (diamond markers) is obtained by subtracting the area of the annulus where the air gap around the contact is thinner than 4 μm, as illustrated in Fig. 10.

Beyond the uncertainty introduced by the presence of the streak artifacts of Fig. 5, the measurement of A_R is also very sensitive to the resolution used to capture our 3D volumes. Fig. 8 shows the evolution of A_R during loading, as obtained by segmentation and surface reconstruction performed on the same original volumes with two different voxel sizes: (i) 8 μm/voxel (blue circles) and (ii) 4 μm/voxel (blue triangles). Both segmentations provided a contact area significantly larger than the one obtained from the optical measurement (purple line). However, the overestimation of A_R decreases when the voxel size also decreases.

The origin of this overestimation results from the partial volume effect and its consequences on the segmentation results, based on the Random Walker Algorithm Grady, 2006 in this work. Fig. 9 illustrates these effects on the segmentation of a theoretical Hertzian contact profile (Hertz, 1881) at three different voxel sizes: 4 μm, 8 μm and 16 μm. The partial volume effect, due to the discreteness of the pixels in the images, tends to blur or average the pixel gray level in regions of the sample with strong gradients in attenuation of the X-rays (i.e. at the interface between different phases). The border of the contact region, with a triple line joining air, PDMS and PMMA, followed by a very thin layer of air between PDMS and PMMA, is a region where such partial volume *blurring* effect can have strong consequences on the apparent contact radius if the voxel size is not small enough. Figs. 9.c–e show that the blurring is significant when the contact opening is less than the voxel size. This makes it impossible to place air markers (for random walker segmentation) arbitrarily close to the contact edge. This results in an error in the position of the contact edge after segmentation, due to an easier diffusion from the PMMA and PDMS markers in the region where air markers are absent. This error, which is directly linked to the distance between the last air marker and the edge of the contact, increases dramatically when the voxel size increases (from 4 μm in Fig. 9.f to 16 μm in Fig. 9.h). In the schematic and theoretical example of Fig. 9, the error is of the order of 10 times the voxel size. As a consequence, one can expect an accurate direct measurement of A_R only for very high resolution. Note that any other segmentation procedure would also suffer from the partial volume effect in the vicinity of the contact edge and the resulting blurring of gray levels. As a matter of fact, the Random Walker algorithm adopted here was identified as the most efficient to perform the segmentation operation at a given resolution, among the many procedures available for example in the `scikit-image` package (Walt et al., 2014).

As the smallest voxel size available in our case was of 4 μm, we propose an alternative method to achieve accurate estimation based on a theoretical correction of the experimental measurement. This method will also account for the remaining difference with the optical measurement, observed in Fig. 8. Fig. 10(a) shows the theoretical shape of a deformed sphere on a rigid plane according to the Hertz contact model (Hertz, 1881) at two indentations: 32 μm and 152 μm. In this representation, the real contact area corresponds to the plateau at $z = 0$ and the air gap of increasing thickness is located under the curve. We can then consider that, depending on resolution, the apparent position of the contact edge (as detected by the segmentation procedure) corresponds to the position of the theoretical profile at an altitude (z) approximately equal to the voxel size (see the vertical dashed lines crossing the profile at a 4 μm or 8 μm offset from the contact surface $z = 0$). The result is that the apparent contact radius $\hat{a}$ (the length of the horizontal plateau at $z = 4$ or 8 μm) extends up to the dashed lines and thus includes an additional contribution Δr to the theoretical contact radius a_H. As the Δr depends on the normal indentation δ, we obtain:

$$\Delta r(\delta) = \hat{a}(\delta) - a_H(\delta). \tag{1}$$

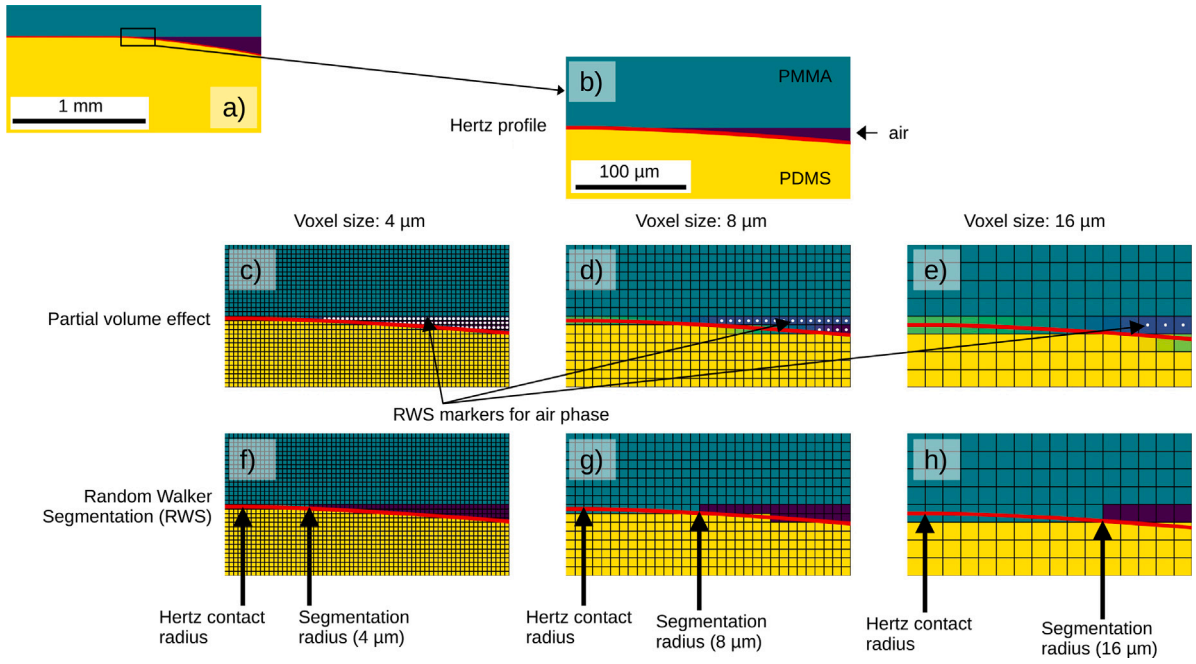

Fig. 9. Evolution of the contact edge position as a function of the image resolution. (a)–(b) Theoretical Hertz profile of a deformed sphere (R = 9.42 mm, δ = 152 µm) (c)–(e) Partial volume effect at increasing voxel size, from 4 µm to 16 µm. The blurring of gray levels near the contact zone (pixels are averaged between green (PMMA) and yellow (PDMS)) tends to shift the last air marker (white points) away from the contact edge when the voxel size increases. (f)–(h) Random Walker segmentation result. The contact radius is overestimated as the PDMS and PMMA phases diffuse abnormally in the blurred region where air markers are absent. The contact region shown in panels (c) to (h) is the same as that in (b). (For interpretation of the references to color in this figure legend, the reader is referred to the web version of this article.)

We can evaluate now the additional contribution A_{add} to the theoretical Hertzian contact area A_H :

$$A(\delta) = \pi\left(a_H(\delta)+\Delta r(\delta)\right)^2 = A_H(\delta)+\pi\left(2\cdot\Delta r(\delta)\cdot a_H(\delta)+\Delta r^2\right) = A_H(\delta)+A_{add} \tag{2}$$

Assuming for simplicity, that the real contact is close enough to the theoretical Hertzian contact area, we can subtract the computed value of A_{add} for each indentation step from our experimental data. The result is plotted in Fig. 9 (blue diamonds) and is now nearly linear (intercept is close to 0) and in very good agreement with the optical measurement. The value of the intercept is now fully compatible with the very low work of adhesion extracted during loading in the optical experiment (see Table 1). Finally, Fig. 10(b) displays how A_{add} evolves as a function of the contact radius and the image resolution. This error in the estimation of the contact radius (and then on the contact area), due to the very thin layer of air close to the contact edge, could rapidly grow to very high values when increasing the voxel size. Conversely, this relative error is decreasing with the contact radius for a given image resolution, indicating that optimizing the accuracy of A_R measurements requires the use of the finest possible spatial resolution.

3.2. Deformation profiles

Let us now emphasize another important feature of XRCT measurements, not available with a simple 2D optical observation, which is the access to the complete morphology of the deformed bodies involved in a contact. As already shown before, image segmentation enables the extraction of the profile of the surface of our deformed PDMS, even outside of the contact. Fig. 11 shows, during loading and unloading, the shape of the deformed PDMS sample at three different indentations, in a vertical XZ plane passing through the center of the specimen. The profiles are obtained by radially averaging the position of the PDMS surface around the contact center as the profiles are symmetric with respect to 0. We can clearly see how the PDMS is deforming as soon as the sample is moved in the Z-direction against the PMMA plane (represented here at $z = 0$) and how it retrieves its initial shape during unloading.

It is possible to extract the surface displacement fields of the deformed sample by subtracting the original undeformed shape of the PDMS hemisphere from the deformed profiles. Fig. 12 shows the experimental surface displacement fields as colored bands for three different indentation steps during loading (δ = 72, 112 and 152 µm) and unloading (δ = 132, 72 and 37 µm). The width of the colored bands corresponds to twice the typical size of a voxel (here 4 µm) in order to underline that the experimental surface profile is presumably positioned within an error margin of at least one voxel, depending on the different factors discussed above affecting the blurring of the interface and the accuracy of segmentation. Fig. 12 also shows the corresponding theoretical displacement profiles for the three contact models introduced in Section 2.3.2: JKR (green lines), DMT (purple lines) and Maugis–Dugdale (black lines).

The model profiles were obtained according to equations (7.3) and (7.6) from the work of Maugis (1992) and using the values of the Young's modulus E, the work of adhesion w and the Tabor parameter λ from the optical experiment (see Table 1). To account for the uncertainty on all three parameters, we adopted a Monte Carlo based method. We first performed 10 000 Gaussian draws with the same mean value and standard deviation as in Table 1 for the three parameters E, w and λ. We then evaluated both the mean position of those 10 000 profiles and their standard deviation. The included error bars for the theoretical curves are intended to be three times the standard deviation obtained for each profile.

The experimental data are in good quantitative agreement with the predictions of the three models, especially at large indentation. Slight deviations are nevertheless observed for low indentation values, especially during unloading. The origin of these discrepancies may be linked to the unavoidable experimental differences between the XRCT and the optical experiments that were used to extract the mechanical and adhesive properties of PDMS. Both experiments were carried out on different mechanical devices differing in terms of stiffness (which may affect the effective indentation). Moreover, the temperature in

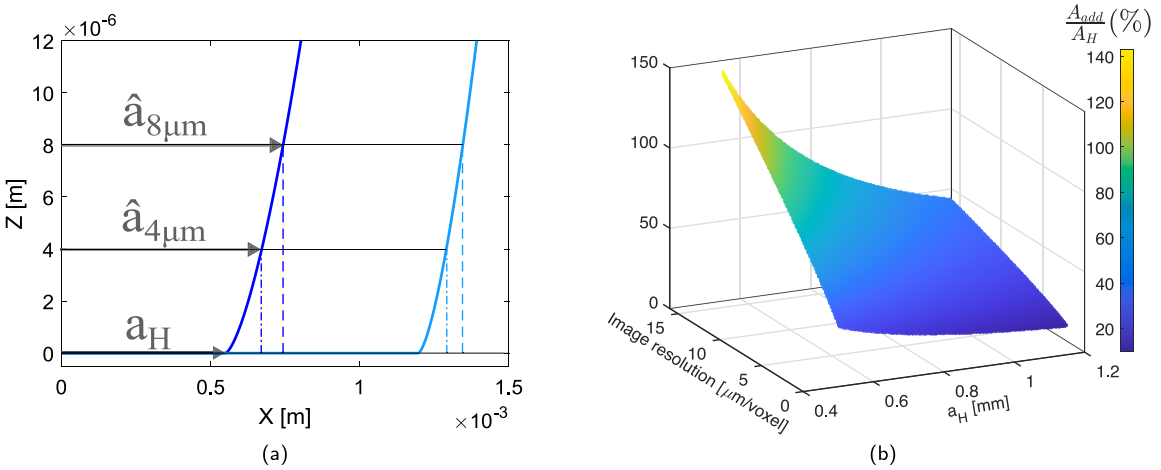

Fig. 10. Theory-based correction of the experimental measurement : (a) Deformation of the surface of a sphere (R = 9.42 mm) according to Hertz's displacement field, for an indentation of 32 μm (dark blue) and 152 μm (light blue). $\hat{a}_{4\mu m}$ and $\hat{a}_{8\mu m}$ represent the smallest contact radii detectable with each corresponding resolution. (b) Evolution of the relative area error A_{add}/A_H (as calculated using Eq. (2)), as a function of both the Hertz contact radius and the voxel size (the typical offset from the contact surface). (For interpretation of the references to color in this figure legend, the reader is referred to the web version of this article.)

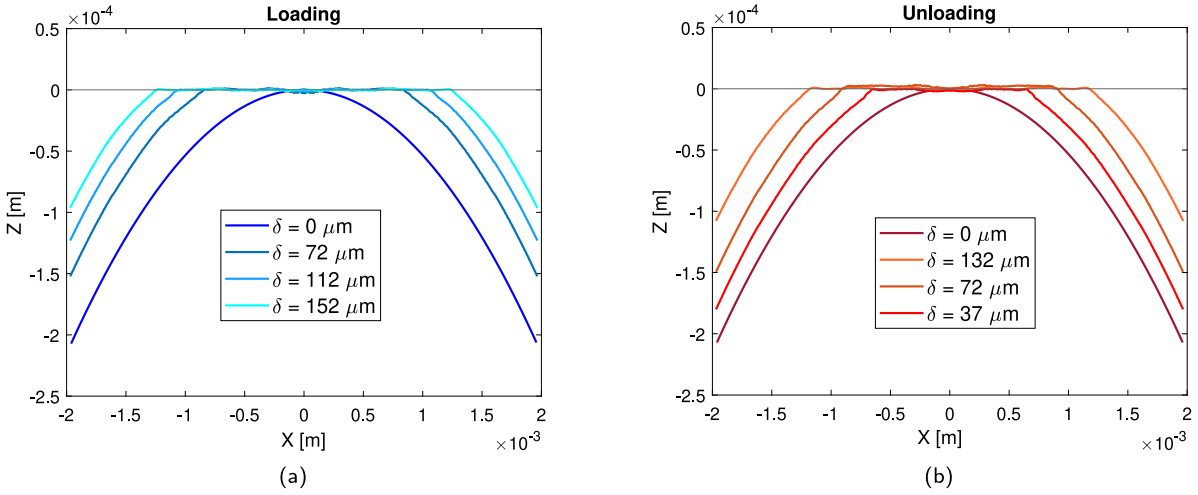

Fig. 11. Shape of the deformed PDMS surface as a function of the normal indentation during (a) loading and (b) unloading. Only 3 indentation steps are represented for simplicity, together with the non-deformed case ($\delta = 0$). The profiles correspond to the radially-averaged position of the PDMS surface around the contact center (the profiles are symmetric with respect to 0).

the XRCT device is not controlled and may rise by a few degrees during the volume acquisition, which may affect the mechanical and adhesive properties of the PDMS specimen. Thus, the evaluation of the fit parameters used to calculate the theoretical profiles may not be fully representative of the experimental conditions during XRCT.

Focusing on the theoretical profiles, one can observe that the profiles from the three models are very similar during loading for all indentation steps. The differences are slightly larger during unloading, especially in the vicinity of the contact edge. In particular, the JKR profile exhibits the expected neck formed at the contact edge due to the short-ranged adhesion forces on a deformable solid (Barthel, 2008). In the conditions used during our experiments, those effects have a limited amplitude and remain confined at the very vicinity of the contact edge. Thus, the resolution of our tomography measurements is not fine enough to discriminate among them (the differences between the models are smaller than the width of the colored bands in Fig. 12). While we leave the details of the discussion on the physics and modeling of adhesive contact for a future paper, our work allows us to conclude that a high resolution is required to capture both (i) a precise measurement of the contact area and (ii) an accurate surface deformation profile in the vicinity of the contact edge.

4. Conclusions

The tomography approach presented in this work opens new opportunities in experimental tribology with access to *in situ* contact mechanics in 3D and for potentially optically opaque materials. It was applied here to an ideal system consisting of a soft PDMS hemisphere in quasi-static contact with a stiff PMMA plane under normal loading.

The procedure developed, based on *in situ* mechanical testing under X-ray computed tomography, image segmentation and surface reconstruction, allows for characterization of the real contact non-destructively and in three dimensions. This gives a 3D experimental access to two fundamental quantities in contact mechanics: the real contact area A_R and the displacement field of the deformed surfaces, the latter being inaccessible up to now with the standard *in situ* optical contact monitoring techniques. These two quantities can be easily compared to the predictions of established analytical linearly elastic

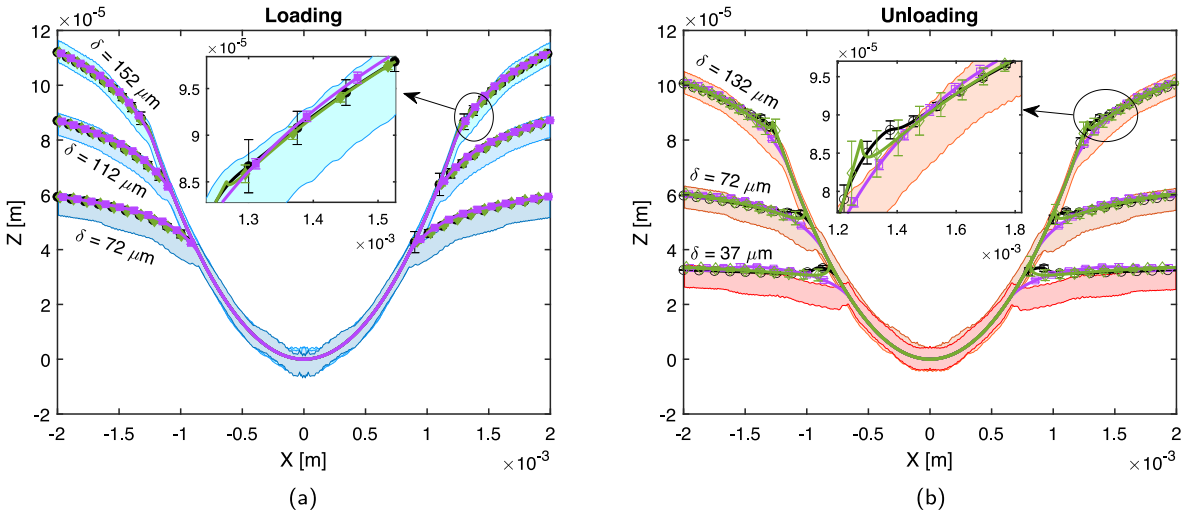

Fig. 12. Surface displacement field for the three indentations shown in Fig. 11 during loading (a) and unloading (b). The colored bands are the XRCT experimental results where the bandwidth is twice the voxel size (4 μm). Solid lines are the theoretical profiles calculated with the Maugis–Dugdale (black), JKR (green) and DMT (purple) models. The necessary model parameters are the ones provided in Table 1. The symbols and colors are the same as in Fig. 6. Error bars: see text. (For interpretation of the references to color in this figure legend, the reader is referred to the web version of this article.)

adhesive contact models, such as JKR, DMT and Maugis–Dugdale models.

The comparison of the 3D measurement of the real contact area against the reference (2D) optical procedure highlights a systematic tendency of the 3D procedure to overestimate the contact area. This is directly related to the resolution of the tomography experiment and to the different mechanisms tending to average the material and interface information at the scale of one voxel in the vicinity of the contact edge.

A correction of the 3D contact radius was proposed based on the theoretical Hertzian contact profile, allowing to retrieve the reference values measured in the optical procedure. Alternatively, the use of high-resolution tomography is likely to reduce the discrepancy between the 2D and 3D measurements.

The particular configuration studied here also highlights the presence of potential tomography artifacts in the vicinity of the contact zone, affecting the accuracy of the contact area measurement. These are related to the phase shift of the X-rays in the vicinity of the contact region.

The detailed analysis of the ideal sphere-on-plane contact system carried out in this work shows that a high resolution in the vicinity of the contact edge is the key to both an accurate measurement of A_R and to the potential discrimination between theoretical contact models, in particular concerning their predictions of the surface displacement field. As a forthcoming perspective, some experiments under an X-ray Synchrotron beam could be a solution for having a better image resolution. Another direct perspective of the present work would be to provide new experimental measurements to test already existing theoretical models for more realistic non-transparent, rough and/or stiffer materials encountered in many applications such as tire–road contact, sealing, bearings or haptic devices.

CRediT authorship contribution statement

Vito Acito: Methodology, Software, Investigation, Formal analysis, Data curation, Writing – original draft, Visualization. **Sylvain Dancette:** Conceptualization, Software, Formal analysis, Writing – original draft, Supervision, Funding acquisition. **Julien Scheibert:** Conceptualization, Validation, Writing – review & editing. **Cristobal Oliver:** Investigation. **Jérome Adrien:** Methodology, Investigation, Resources. **Eric Maire:** Validation, Writing – review & editing. **Davy Dalmas:** Conceptualization, Software, Formal analysis, Writing – original draft, Supervision, Funding acquisition.

Declaration of competing interest

The authors declare that they have no known competing financial interests or personal relationships that could have appeared to influence the work reported in this paper.

Data availability

The raw/processed data required to reproduce these findings cannot be shared at this time as the data also forms part of an ongoing study.

Acknowledgments

The authors thank Emilie Delplanque and Nazario Morgado (LTDS, Ecole Centrale de Lyon) for their help in the specimen fabrication, and Antoine Aymard (LTDS, Ecole Centrale de Lyon) for his help in the optical experiments and discussions.

Funding

This work was supported by the LABEX MANUTECH-SISE (ANR-10-LABX-0075) of Université de Lyon, within the Plan France 2030 operated by the French National Research Agency (ANR). This work was also supported by LABEX iMUST (Grant No. ANR-10-LABX-0064) of Université de Lyon within the program “Investissements d’Avenir” (Grant No. ANR-11-IDEX-0007) operated by the French National Research Agency (ANR) and by ANR through Grant ANR-21-CE06-0048 (WEEL project).

References

Acito, Vito, Ciavarella, Michele, Prevost, Alexis M., Chateauminois, Antoine, 2019. Adhesive contact of model randomly rough rubber surfaces. Tribol. Lett. 67 (2), 54. http://dx.doi.org/10.1007/s11249-019-1164-9.

Aghababaei, Ramin, Warner, Derek H., Molinari, Jean-François, 2017. On the debris-level origins of adhesive wear. Proc. Natl. Acad. Sci. 114 (30), 7935–7940. http://dx.doi.org/10.1073/pnas.1700904114.

Aleksejev, Jure, Lim, Yijun, Huber, John, Hofmann, Felix, Marrow, James, 2020. In-situ X-ray tomography of wear – A feasibility study. Tribol. Int. 150, 106355. http://dx.doi.org/10.1016/j.triboint.2020.106355.

Barrett, Julia F., Keat, Nicholas, 2004. Artifacts in CT: Recognition and avoidance. RadioGraphics 24 (6), 1679–1691. http://dx.doi.org/10.1148/rg.246045065.

Barthel, E., 2008. Adhesive elastic contacts: JKR and more. J. Phys. D: Appl. Phys. 41 (16), 163001. http://dx.doi.org/10.1088/0022-3727/41/16/163001.

Bowden, F.P., Tabor, D., 1942. Mechanism of metallic friction. Nature 150 (3798), 197–199. http://dx.doi.org/10.1038/150197a0, Number: 3798.

Buffiere, J.-Y., Maire, E., Adrien, J., Masse, J.-P., Boller, E., 2010. In situ experiments with X ray tomography: an attractive tool for experimental mechanics. Exp. Mech. 50 (3), 289–305. http://dx.doi.org/10.1007/s11340-010-9333-7.

Chateauminois, Antoine, Fretigny, Christian, Olanier, Ludovic, 2010. Friction and shear fracture of an adhesive contact under torsion. Phys. Rev. E 81 (2), 026106. http://dx.doi.org/10.1103/PhysRevE.81.026106.

Chaudhury, Manoj K., Weaver, Timothy, Hui, C.Y., Kramer, E.J., 1996. Adhesive contact of cylindrical lens and a flat sheet. J. Appl. Phys. 80 (1), 30–37. http://dx.doi.org/10.1063/1.362819.

Cloetens, P., Pateyron-Salomé, M., Buffière, J.Y., Peix, G., Baruchel, J., Peyrin, F., Schlenker, M., 1997. Observation of microstructure and damage in materials by phase sensitive radiography and tomography. J. Appl. Phys. 81 (9), 5878–5886. http://dx.doi.org/10.1063/1.364374.

Dalzin, F., Le Bot, A., Perret-Liaudet, J., Mazuyer, D., 2016. Tribological origin of squeal noise in lubricated elastomer–glass contact. J. Sound Vib. 372, 211–222. http://dx.doi.org/10.1016/j.jsv.2016.01.019.

Delplanque, Emilie, Aymard, Antoine, Dalmas, Davy, Scheibert, Julien, 2022. Solving curing-protocol-dependent shape errors in PDMS replication. J. Micromech. Microeng. 32 (4), 045006. http://dx.doi.org/10.1088/1361-6439/ac56ea.

Derjaguin, B.V, Muller, V.M, Toporov, Yu. P., 1975. Effect of contact deformations on the adhesion of particles. J. Colloid Interface Sci. 53 (2), 314–326. http://dx.doi.org/10.1016/0021-9797(75)90018-1.

Dieterich, James H., Kilgore, Brian D., 1994. Direct observation of frictional contacts: New insights for state-dependent properties. Pure Appl. Geophys. 143 (1), 283–302. http://dx.doi.org/10.1007/BF00874332.

Feldkamp, L.A., Davis, L.C., Kress, J.W., 1984. Practical cone-beam algorithm. JOSA A 1 (6), 612–619. http://dx.doi.org/10.1364/JOSAA.1.000612.

Grady, L., 2006. Random walks for image segmentation. IEEE Trans. Pattern Anal. Mach. Intell. 28 (11), 1768–1783. http://dx.doi.org/10.1109/TPAMI.2006.233, Conference Name: IEEE Transactions on Pattern Analysis and Machine Intelligence.

Guibert, M., Oliver, C., Durand, T., Le Mogne, T., Le Bot, A., Dalmas, D., Scheibert, J., Fontaine, J., 2021. A versatile flexure-based six-axis force/torque sensor and its application to tribology. Rev. Sci. Instrum. 92 (8), 085002. http://dx.doi.org/10.1063/5.0057266.

Hertz, H., 1881. Über die Berührung fester elastischer Körper. J. Reine Angew. Math. 92, 156–171.

Johnson, K.L., 1987. Contact mechanics. Cambridge University Press.

Johnson, Kenneth Langstreth, Kendall, Kevin, Roberts, A.D., 1971. Surface energy and the contact of elastic solids. Proc. R. Soc. Lond. Ser. A Math. Phys. Eng. Sci. 324 (1558), 301–313. http://dx.doi.org/10.1098/rspa.1971.0141.

Krick, Brandon A., Vail, Jennifer R., Persson, Bo N.J., Sawyer, W. Gregory, 2012. Optical in situ micro tribometer for analysis of Real Contact Area for contact mechanics, adhesion, and sliding experiments. Tribol. Lett. 45 (1), 185–194. http://dx.doi.org/10.1007/s11249-011-9870-y.

Kriston, András, Fülöp, Tibor, Isitman, Nihat Ali, Kotecký, Ondřej, Tuononen, Ari J., 2016. A novel method for contact analysis of rubber and various surfaces using micro-computerized-tomography. Polym. Test. 53, 132–142. http://dx.doi.org/10.1016/j.polymertesting.2016.05.019.

Lengiewicz, J., de Souza, M., Lahmar, M.A., Courbon, C., Dalmas, D., Stupkiewicz, S., Scheibert, J., 2020. Finite deformations govern the anisotropic shear-induced area reduction of soft elastic contacts. J. Mech. Phys. Solids 143, 104056. http://dx.doi.org/10.1016/j.jmps.2020.104056.

Lorensen, William E., Cline, Harvey E., 1987. Marching cubes: A high resolution 3D surface construction algorithm. ACM SIGGRAPH Comput. Graph. 21 (4), 163–169. http://dx.doi.org/10.1145/37402.37422.

Maugis, Daniel, 1992. Adhesion of spheres: The JKR-DMT transition using a dugdale model. J. Colloid Interface Sci. 150 (1), 243–269. http://dx.doi.org/10.1016/0021-9797(92)90285-T.

Medina, S., Nowell, D., Dini, D., 2013. Analytical and numerical models for tangential stiffness of rough elastic contacts. Tribol. Lett. 49 (1), 103–115. http://dx.doi.org/10.1007/s11249-012-0049-y.

Mengaldo, Gianmarco, Renda, Federico, Brunton, Steven L., Bächer, Moritz, Calisti, Marcello, Duriez, Christian, Chirikjian, Gregory S., Laschi, Cecilia, 2022. A concise guide to modelling the physics of embodied intelligence in soft robotics. Nat. Rev. Phys. 4 (9), 595–610. http://dx.doi.org/10.1038/s42254-022-00481-z, Number: 9.

Mergel, Janine C., Sahli, Riad, Scheibert, Julien, Sauer, Roger A., 2019. Continuum contact models for coupled adhesion and friction. J. Adhes. 95 (12), 1101–1133. http://dx.doi.org/10.1080/00218464.2018.1479258, arXiv:1803.00046.

Müser, Martin H., Dapp, Wolf B., Bugnicourt, Romain, Sainsot, Philippe, Lesaffre, Nicolas, Lubrecht, Ton A., Persson, Bo N.J., Harris, Kathryn, Bennett, Alexander, Schulze, Kyle, Rohde, Sean, Ifju, Peter, Sawyer, W. Gregory, Angelini, Thomas, Ashtari Esfahani, Hossein, Kadkhodaei, Mahmoud, Akbarzadeh, Saleh, Wu, Jiunn-Jong, Vorlaufer, Georg, Vernes, András, Solhjoo, Soheil, Vakis, Antonis I., Jackson, Robert L., Xu, Yang, Streator, Jeffrey, Rostami, Amir, Dini, Daniele, Medina, Simon, Carbone, Giuseppe, Bottiglione, Francesco, Afferrante, Luciano, Monti, Joseph, Pastewka, Lars, Robbins, Mark O., Greenwood, James A., 2017. Meeting the contact-mechanics challenge. Tribol. Lett. 65 (4), 118. http://dx.doi.org/10.1007/s11249-017-0900-2.

Pérez-Ràfols, Francesc, Nicola, Lucia, 2022. Incipient sliding of adhesive contacts. Friction 10 (6), 963–976. http://dx.doi.org/10.1007/s40544-021-0546-9.

Persson, B.N.J., Albohr, O., Tartaglino, U., Volokitin, A.I., Tosatti, E., 2004. On the nature of surface roughness with application to contact mechanics, sealing, rubber friction and adhesion. J. Phys.: Condens. Matter 17 (1), R1. http://dx.doi.org/10.1088/0953-8984/17/1/R01.

Popov, Valentin L., 2017. Contact Mechanics and Friction. Springer, http://dx.doi.org/10.1007/978-3-662-53081-8.

Prevost, A., Scheibert, J., Debrégeas, G., 2013. Probing the micromechanics of a multi-contact interface at the onset of frictional sliding. Eur. Phys. J. E 36 (2), 17. http://dx.doi.org/10.1140/epje/i2013-13017-0.

Putignano, Carmine, Menga, Nicola, Afferrante, Luciano, Carbone, Giuseppe, 2019. Viscoelasticity induces anisotropy in contacts of rough solids. J. Mech. Phys. Solids 129, 147–159. http://dx.doi.org/10.1016/j.jmps.2019.03.024.

Rubinstein, Shmuel M., Shay, Meni, Cohen, Gil, Fineberg, Jay, 2006. Crack-like processes governing the onset of frictional slip. Int. J. Fract. 140 (1), 201–212. http://dx.doi.org/10.1007/s10704-006-0049-8.

Sahli, R., Pallares, G., Ducottet, C., Ben Ali, I.E., Al Akhrass, S., Guibert, M., Scheibert, J., 2018. Evolution of real contact area under shear and the value of static friction of soft materials. Proc. Natl. Acad. Sci. 115 (3), 471–476. http://dx.doi.org/10.1073/pnas.1706434115.

Sahli, R., Pallares, G., Papangelo, A., Ciavarella, M., Ducottet, C., Ponthus, N., Scheibert, J., 2019. Shear-induced anisotropy in rough elastomer contact. Phys. Rev. Lett. 122 (21), 214301. http://dx.doi.org/10.1103/PhysRevLett.122.214301.

Sanner, Antoine, Pastewka, Lars, 2022. Crack-front model for adhesion of soft elastic spheres with chemical heterogeneity. J. Mech. Phys. Solids 160, 104781. http://dx.doi.org/10.1016/j.jmps.2022.104781.

Scheibert, J., Leurent, S., Prevost, A., Debrégeas, G., 2009. The role of fingerprints in the coding of tactile information probed with a biomimetic sensor. Science 323 (5920), 1503–1506. http://dx.doi.org/10.1126/science.1166467.

Tabor, D., 1977. Surface forces and surface interactions. In: Kerker, Milton, Zettlemoyer, Albert C., Rowell, Robert L. (Eds.), Plenary and Invited Lectures. Academic Press, pp. 3–14. http://dx.doi.org/10.1016/B978-0-12-404501-9.50009-2.

Vakis, A.I., Yastrebov, V.A., Scheibert, J., Nicola, L., Dini, D., Minfray, C., Almqvist, A., Paggi, M., Lee, S., Limbert, G., Molinari, J.F., Anciaux, G., Aghababaei, R., Echeverri Restrepo, S., Papangelo, A., Cammarata, A., Nicolini, P., Putignano, C., Carbone, G., Stupkiewicz, S., Lengiewicz, J., Costagliola, G., Bosia, F., Guarino, R., Pugno, N.M., Müser, M.H., Ciavarella, M., 2018. Modeling and simulation in tribology across scales: An overview. Tribol. Int. 125, 169–199. http://dx.doi.org/10.1016/j.triboint.2018.02.005.

Violano, Guido, Chateauminois, Antoine, Afferrante, Luciano, 2021. A JKR-like solution for viscoelastic adhesive contacts. Front. Mech. Eng. 7, http://dx.doi.org/10.3389/fmech.2021.664486.

Walt, Stéfan van der, Schönberger, Johannes L., Nunez-Iglesias, Juan, Boulogne, François, Warner, Joshua D., Yager, Neil, Gouillart, Emmanuelle, Yu, Tony, 2014. Scikit-image: image processing in Python. PeerJ 2, e453. http://dx.doi.org/10.7717/peerj.453.

Withers, Philip J., Bouman, Charles, Carmignato, Simone, Cnudde, Veerle, Grimaldi, David, Hagen, Charlotte K., Maire, Eric, Manley, Marena, Du Plessis, Anton, Stock, Stuart R., 2021. X-ray computed tomography. Nat. Rev. Methods Primers 1 (1), 1–21. http://dx.doi.org/10.1038/s43586-021-00015-4, Number: 1.

Wu, Ziji, Sullivan, Jr., John M., 2003. Multiple material marching cubes algorithm. Internat. J. Numer. Methods Engrg. 58 (2), 189–207. http://dx.doi.org/10.1002/nme.775, _eprint: https://onlinelibrary.wiley.com/doi/pdf/10.1002/nme.775.

Zhang, Feikai, Liu, Jianhua, Ding, Xiaoyu, Wang, Runliang, 2019. Experimental and finite element analyses of contact behaviors between non-transparent rough surfaces. J. Mech. Phys. Solids 126, 87–100. http://dx.doi.org/10.1016/j.jmps.2019.02.004.

Zhang, Feikai, Liu, Jianhua, Ding, Xiaoyu, Yang, Zhimeng, 2020. A discussion on the capability of X-ray computed tomography for contact mechanics investigations. Tribol. Int. 145, 106167. http://dx.doi.org/10.1016/j.triboint.2020.106167.